# Towards subpicosecond pulses from solid target plasma based seeded soft X-ray laser

Alok Kumar Pandey, Alok Kumar Pandey, Irene Papagiannouli, Fabrice Sanson, Elsa Baynard, Julien Demailly, Sophie Kazamias, Moana Pittman, Olivier Neveu, Bruno Lucas, et al.

Research Article | Vol. 28, No. 20 / 28 September 2020 / Optics Express 28924
Optics EXPRESS

# Towards subpicosecond pulses from solid target plasma based seeded soft X-ray laser

ALOK KUMAR PANDEY,[1] IRENE PAPAGIANNOULI,[1] FABRICE SANSON,[1] ELSA BAYNARD,[1] JULIEN DEMAILLY,[1] SOPHIE KAZAMIAS,[1] MOANA PITTMAN,[1] OLIVIER NEVEU,[1] BRUNO LUCAS,[1] ANDREA LE MAREC,[2] ANNIE KLISNICK,[2] ANNETTE CALISTI,[3] OLIVIER LARROCHE,[4] DAVID ROS,[1] AND OLIVIER GUILBAUD[1,*]

[1]*Laboratoire Irène Joliot-Curie, Université Paris-Saclay , UMR CNRS, Rue Ampère, Bâtiment 200, F-91898, Orsay Cedex, France*
[2]*Institut des Sciences Moléculaires d'Orsay, Université Paris-Saclay , UMR CNRS 8214, Rue André Rivière, Bâtiment 520, 91405 Orsay Cedex, France*
[3]*Aix-Marseille Université, CNRS, Physique des Interactions Ioniques et Moléculaires, Centre Saint-Jérôme, F-13397 Marseille cedex 20, France*
[4]*CEA DAM DIF, 91297 Arpajon, Cedex, France*
[*]*olivier.guilbaud@u-psud.fr*

**Abstract:** We investigate the coherence of plasma-based soft X-ray laser (XRL) for different conditions that can alter the electron density in the gain region. We first measure the source temporal coherence in amplified spontaneous emission (ASE) mode. We develop a data analysis procedure to extract both its spectral width and pulse duration. These findings are in agreement with the spectral line shape simulations and seeded operation experimental results. Utilizing the deduced spectral width and pulse duration in a one-dimensional Bloch-Maxwell code, we reproduce the experimental temporal coherence properties of the seeded-XRL. Finally, we demonstrate efficient lasing in ASE and seeded mode at an electron density two times higher than the routine conditions. In this regime, using Bloch-Maxwell modeling, we predict the pulse duration of the seeded XRL to be ~500*fs*.



## 1. Introduction

Spectro-temporal metrology of light pulses is at the center of the dramatic progress of ultra-short lasers. it is now instrumental in the rapid development of short, coherent, and intense soft X-ray sources such as X-ray free-electron lasers (XFEL), Laser high order harmonics (HH) and plasma-based soft X-ray lasers (XRL). In an endeavor to reduce the XRL pulse duration, it has been proposed to use XRL amplifiers performing at high electron densities. Seeded operation of XRL in a high-density gas target has been demonstrated, with clear evidence of gain lifetime shortening due to increased ionization rate by collisions [1]. This work opened a path towards high energy, extreme ultraviolet (EUV) pulses with hundreds of femtoseconds pulse duration at high repetition rate laser drivers. However, no direct evidence of pulse duration shortening has been so far reported. In this wavelength range, temporal profile characterization requires indeed sophisticated non-linear autocorrelation or cross-correlation techniques involving multi-photon ionization processes. In this matter, measuring the first-order autocorrelation function through interferometry is usually of limited help as it gives only access to the spectral intensity and not to the spectral phase. However, such a temporal coherence study may confirm the successful generation of gain at higher density by providing evidence of a bandwidth increase with electron density.

In order to extract some quantitative estimations from such a measurement, some precautions have to be taken. First, the intrinsic bandwidth of the lasing transition will be reduced during the

#399339 https://doi.org/10.1364/OE.399339
Journal © 2020 Received 10 Jun 2020; revised 26 Aug 2020; accepted 26 Aug 2020; published 15 Sep 2020

Optics EXPRESS

amplification process. Besides, in seeded mode, the nonadiabatic response of the gain medium can induce spectral structures through the Rabi oscillation process. If the measurement is performed in the unseeded regime, the shot-to-shot stochastic structures of amplified spontaneous emission (ASE) pulses, will have consequences on the statistical properties of the first-order autocorrelation function, exacerbated when the inverse of the bandwidth is close to the pulse duration. This effect has been recently discussed by LeMarec et al. [2,3]. The pulse structure is expected to be a stochastic succession of spikes of similar duration, modulated by a longer duration envelope. The resulting autocorrelation also will present stochastic shot-to-shot fluctuations, vanishing when averaged over many pulses. Because in the most experimental setups, only the modulus of the linear autocorrelation function is measured through the visibility of the fringes, the stochastic fluctuation will persist after averaging. It then becomes possible to extract both the envelope and spike duration, the latter being related to the Fourier limited duration and the inverse of the average spectral bandwidth.

We present in this paper the experimental characterization of the XRL temporal coherence in different pumping configurations expected to affect the electron density in the gain region. This experiment has been performed in both ASE and seeded regime. When the XRL was operated in ASE mode, the temporal coherence results have been compared to the prediction of the aforementioned model describing the ASE field statistical properties. This comparison is carried out with a fitting procedure first benchmarked on the field model and then applied to the experimental data. The fitting method grants access both to the spectral bandwidth and the duration of the XRL pulse. We show that the deduced values are in good agreement with the results of the spectral lineshape model and with the amplification dynamics observed during the seeded operation of XRL. Using these parameters in a one dimension Bloch-Maxwell model, it was possible to simulate the first-order autocorrelation function of the seeded-XRL amplifier. We show that the numerical results are in good agreement with experimental observations. Starting from a standard pumping configuration, this work has been extended to the conditions that are expected to increase the electron density in the plasma gain region by a factor of two. Efficient lasing has been demonstrated both in ASE and seeded regime. The temporal coherence analysis confirms a laser gain generated at higher density and Bloch-Maxwell simulation predicts the achievement of $\sim 500fs$ pulse duration during the seeded operation. The possibility of lasing over a large density range opens a feasible path to decrease the pulse duration of solid-target plasma-based XRL far below $1ps$.

## 2. Experimental setup

The 10Hz XRL source considered in this work is a Ne-like Titanium XRL generated at the LASERIX facility [4]. The schematic of the exprimental setup is presented in Fig. 1. The lasing medium consists of an elongated laser-produced plasma in which Ne-like Titanium ions are excited by the plasma hot electrons through transient collisional excitation [5–8]. A rapid electron heating is achieved by irradiating the plasma with an intense picosecond laser pulse. A transient population inversion is obtained between the $3p - 3s$ (J = 0 - 1) ionic transition, corresponding to a lasing wavelength of $\lambda = 32.6nm$. The laser gain is sufficiently high to achieve saturation in less than 3mm propagation in the plasma. Besides, because of the low ion temperature involved in this XRL scheme, the intrinsic laser linewidth is expected to be dominated by homogeneous broadening and thus mostly controlled by the electron density in the plasma gain region. The lasing plasma is obtained in two steps [4,9]. First, a $10ns$ full width at half maximum (FWHM) pulse generated by a frequency-doubled 400 mJ Q-switched Nd YAG laser is focused at normal incidence on a 4mm Titanium target using a cylindrical lens to form $5mm \times 80\mu m$ focal line. This pulse turns a thin layer of the solid target into an expanded, low ionization stage ($<Z> \sim 5 - 6$), moderate electron temperature ($T_e \sim 20eV$) preplasma. After a delay of $4ns$ following the temporal peak intensity of preplasma pulse, an intense IR

Optics EXPRESS

pump pulse with an energy of 1.2 J is line-focused on the preformed plasma. The pump pulse duration $T_{IR}$ can be varied in the picosecond range by adjusting the distance between in-vacuum compressor gratings. Additionally, the motorized mirror mounts facilitate in-vacuum adjustment of the grazing-incidence pumping (GRIP) angle $\Phi$ from 18 to 34 degrees. The dimensions of the sagittal line foci are $4.1mm \times 30\mu m$ and $6.2mm \times 30\mu m$ for $\Phi = 22^\circ$ and $\Phi = 32^\circ$, respectively. The line-foci width, uniformity, and parallelism, which are critical to optimal lasing of XRL, are characterized using a high-magnification imaging system. Motorized optomechanics along with the high-magnification imaging system allows in-vacuum adjustment and characterization of the focal lines. Moreover, the relatively thinner focal width of the pump with respect to the preplasma pulse eases the constraints on the spatial superposition of both the line foci. The delay between preplasma and pump pulse is tunable in the range of 0 to $25ns$ using a Q-switched trigger.

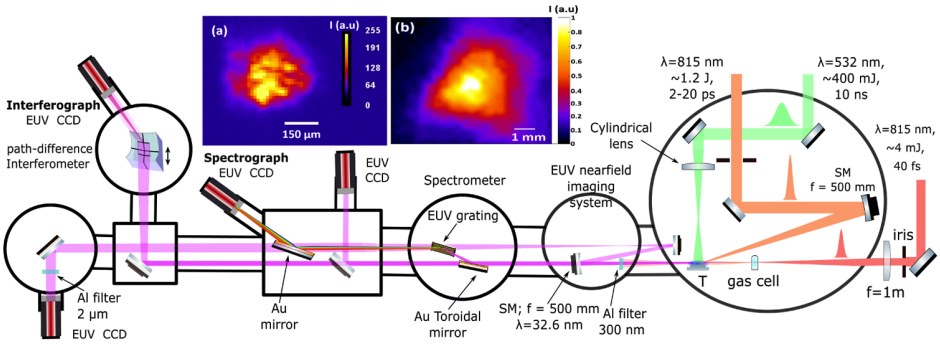


**Fig. 1.** Schematic of the experimental setup. The preplasma is generated by focusing a frequency-doubled Q-switched Nd YAG laser pulse of $10ns$ FWHM duration on the Titanium target (T) using a cylindrical lens. High-energy pump pulse of adjustable duration (tunable between 2 to $20ps$) coming from Ti: Sapphire laser-chain is line-focused on the target using a spherical mirror (SM) of focal length $500mm$. Width, uniformity, and parallelism of the two line-foci are characterized using a high-magnification imaging system (not shown here). The motorized mirror mounts facilitate in-vacuum adjustment of the pump grazing-incidence angle. The diagnostic to the near-field intensity profile of XRL is provided by a EUV imaging system with a magnification of ~12. The inset figure (a) shows the near-field profile of ASE-XRL for $\Phi = 32^\circ$, $T_{IR} = 4ps$. For temporal coherence measurement, the XRL pulse is guided to the path-difference interferometer located ~ $3.2m$ further from the source. For seeded operation, HH seed is generated by focusing an auxiliary low-energy (~4 mJ) infrared beam of pulse duration ~ $40fs$ in a 10 mm long Argon filled gas-cell. Inset figure (b) depicts the seeded-XRL far-field profile acquired on EUV CCD located ~ $1.9m$ from the source for $\Phi = 32^\circ$, $T_{IR} = 4ps$

The pump pulse is incident on the plasma at grazing angle $\Phi$ in order to optimize its absorption. In a simple optical ray-tracing description, its energy is mostly absorbed at the turning point of the ray trajectory, corresponding to a plasma electron density of $N_p = 1.2 \times 10^{21} cm^{-3} sin(\Phi)^2$ [10]. Prior to the temporal coherence, we measured the ASE-XRL signal level for pumping angles $\Phi = 18^\circ$ to $34^\circ$ by a step of $2^\circ$. For each angle, an optimum pump pulse duration $T_{IR}$ yielding maximum signal level in the respective configuration is obtained.

In Table 1, we show the ASE-XRL pulse energy for each experimental condition. Comparing the measured pulse energies, it can be seen that the pump pulse duration $T_{IR} = 4ps$ and $T_{IR} = 7ps$ yields optimal lasing output for $\Phi = 32^\circ$ and $\Phi = 22^\circ$, respectively. Conclusively, for coherence measurement, the grazing angles $\Phi = 22^\circ$ ($N_p = 2 \times 10^{20} cm^{-3}$) and $\Phi = 32^\circ$ ($N_p = 4 \times 10^{20} cm^{-3}$), leading to twice the increase of the electron density in the gain region for the higher angle, have

Optics EXPRESS

been considered. For both the cases, short pulse duration of $T_{IR} = 4ps$ and $T_{IR} = 7ps$ have been investigated, corresponding to optimal lasing output for $\Phi = 32°$ and $\Phi = 22°$ respectively.

**Table 1. Results of the temporal coherence fitting procedure for different values of the grazing angle $\Phi$ and pulse duration $T_{IR}$ of the pumping pulse.**

| $\Phi(\circ)$ | $T_{IR}(ps)$ | $\tau_c(ps)$ | $\tau_{pulse}(ps)$ | $H$ | $ASE-XRL\ energy(\mu J)$ |
|---|---|---|---|---|---|
| 32 | 4 | 1.0 ± 0.1 | 2.1 ±0.2 | 1.0±0.1 | 0.75 |
| 32 | 7 | 1.1 ± 0.1 | 3.0 ±0.4 | 1.0±0.2 | 0.60 |
| 22 | 4 | 1.9± 0.2 | 3.9 ±0.4 | 1.2±0.1 | 0.83 |
| 22 | 7 | 2.6± 0.3 | 5.2 ±0.4 | 1.3±0.2 | 1.1 |

After spectral filtering by a 300nm thick Al filter and a 45° multilayer mirror, the ASE XRL beam was directed toward a wavefront-division interferometer set at a distance of $\sim 3.2m$ from the source. Its conception, described in Appendix A, enables the introduction of a variable path difference $\delta$ between the interfering beamlets without changing their overlapping conditions. The fringe visibility $V$ averaged over multiple single-shot interferograms is represented in Fig. 2 as a function of $\tau = \delta/c$ pertaining to the four experimental configurations previously described; see Appendix B for more details on visibility estimation. Fringe visibility falls faster for $\Phi = 32°$ which is consistent with a relatively higher electron density in the gain region, leading to larger spectral bandwidth and smaller coherence time, as will be discussed in the following section.

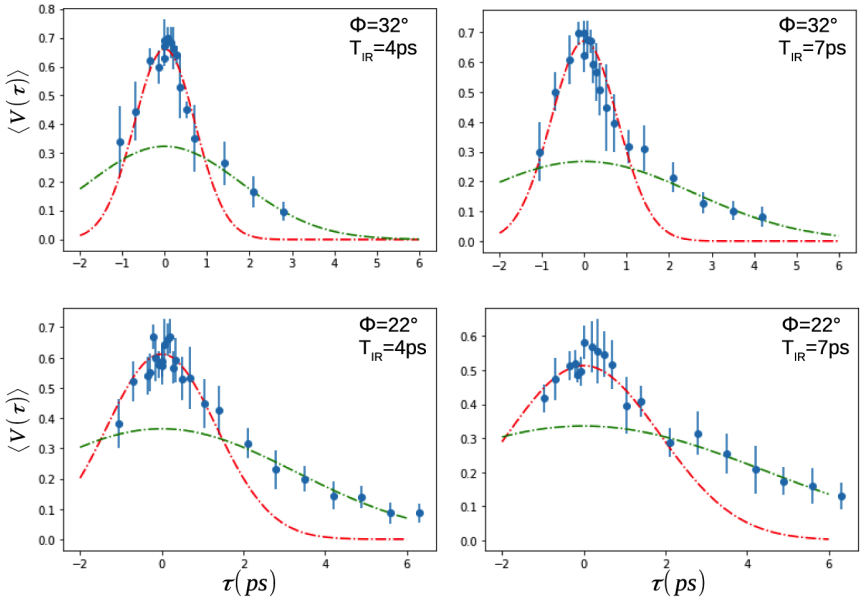


**Fig. 2.** Fringe visibility as a function of relative delay between the interfering beamlets for $\Phi = 32°$ and $\Phi = 22°$ (bottom row). For a given value of $\tau$, the data point is an average of the maximum visibility for 5 to 10 single-shot acquisitions while the error bar represents the standard deviation. The pulse duration $T_{IR}$ is varied by adjusting the distance between in-vacuum compressor gratings. The peak-to-peak delay between preplasma and pumping pulse is $4ns$ in all the cases presented above.

Optics EXPRESS

## 3. Temporal coherence analysis

A quantitative analysis of these results has been performed following the approach proposed by Le Marec et al. [2,3]. The evolution of $V(\tau)$ is compared to the prediction of a stochastic model of ASE pulse-field predicting the characteristics of $<|\gamma(\tau)|>$, the ensemble average of the modulus of the degree of coherence. The function $|\gamma(\tau)|$ is proportional to the fringe visibility $V(\tau)$ and, in the ideal case of a fully coherent and uniform beam, equal to it. Its ensemble average is the ideal limit of an experiment in which a large number of single-shot interferograms can be acquired for each delay $\tau$. More details on the model can be found in [2,11] and in Appendix E. Here we will only describe its structure and its main predictions. In the temporal domain, the pulses are described as a random field of spectral density $S(\nu)$, modulated by a gaussian envelope. We will assume that $S(\nu)$ is gaussian with a FWHM bandwidth $\Delta\nu$. The modulating gaussian envelope has a FWHM in intensity $\tau_{pulse}$, representing the pulse duration. Prediction of the model can be summarised as follows. For small values of $\tau$, the evolution of $<|\gamma(\tau)|>$ will give access to the Fourier transform of $S(\nu)$ which, for a gaussian spectrum is $<|\gamma(\tau)|> = h_0 exp(-(\tau/\tau_c)^2)$, with $h_0 = 1$, and $\tau_c = \frac{2\sqrt{ln2}}{\pi\Delta\nu}$. This behavior is still valid for large values of $\tau$ if the pulse envelope is extremely long or $\tau_{pulse} >> \tau_c$. This asymptotic case corresponds to a stationary random field. For this reason, the parameter $\tau_c$ will be called coherence time. This scenario changes when $\tau_{pulse}$ is close to $\tau_c$. For large values of $\tau$, the $<|\gamma(\tau)|>$ function can be modelled by a gaussian evolution with a width proportional to the pulse envelope: $|\gamma(\tau)| = h_1 exp(-log(2)(\tau/\tau_{pulse})^2)$. In summary, the central part of the $<|\gamma(\tau)|>$ function and its wings can be modelled with separate gaussian functions. From their respective widths, $\Delta\nu$ and $\tau_{pulse}$ can be deduced. Moreover, a relationship exists between the amplitudes of these two gaussian functions: $(h_1/h_0) = C\sqrt{\tau_c/\tau_{pulse}}$, where $C = 0.71$ is a numerical constant (see Appendix E for further details).

In order to compare the prediction of this model to the experimental data, a fitting procedure has been developed. The average experimental visibilities corresponding to delays $-1ps \leqslant \tau \leqslant 1ps$, are fitted with the first gaussian model from which values of $\tau_c$ and $\Delta\nu$ are extracted. These fitting curves are displayed in red in Fig. 2. As the experimental visibility is less than unity for $\tau = 0$, $h_0$ is not fixed to 1 but is considered as a fitting parameter. For $\tau > 1ps$, data points are fitted with the second gaussian model displayed by the green curve in Fig. 2. From the width of this curve, pulse duration $\tau_{pulse}$ is obtained. We show the results of this analysis in Table 1 for different experimental configurations. As explained above, the model also yields the dependence of relative heights of the gaussian functions to the ratio $\tau_{pulse}/\tau_c$. This prediction has been tested by calculating the ratio $H = \frac{h_1/h_0}{C}\sqrt{\tau_{pulse}/\tau_c}$, which should be close to unity if the height relationship is satisfied. The result of this study is presented in Table 1 for each configuration.

As can be seen in Fig. 2, the fitting curves are modelling the experimental data trends very well, particularly the prolonged gradual decrease of the visibility with large $\tau$. Besides, this fitting procedure by two gaussian curves is not arbitrary. Their amplitudes follow the height-relationship, as can be seen from the $H$ values displayed in Table 1, which are deviating from unity by 30% at most. Furthermore, for the same $T_{IR}$, the values of $\tau_c$ and $\tau_{pulse}$ is divided by a factor close to two when $\Phi$ is increased from 22° to 32°. This is consistent with twice the increase of the electron density in the gain region. A higher electron density leads to a larger homogeneous bandwidth, a shorter coherence time $\tau_c$, and a shorter pulse duration $\tau_{pulse}$ due to faster ionization gating [1]. Moreover, for a given angle $\Phi$, a slight decrease of the bandwidth and a small increase of the pulse duration is observed when $T_{IR}$ is increased.

In Table 2 we compare the spectral linewidth $\Delta\nu$ inferred from the measured $\tau_c$ values shown in Table 1 to the linewidth calculated by a spectral line shape model. The PPP code [12,13] has been used to model the homogeneous intrinsic linewidth of the lasing transition for different sets of electron densities $N_e$ and electron temperatures $T_e$. A Doppler inhomogeneous component is also taken into account for the final intrinsic line width. The results of these calculations can be

Optics EXPRESS

found in Appendix D. The evolution of the line profile with the amplification length is calculated following Koch et al. [14]. For the range of plasma parameters corresponding to our experimental conditions, the final lineshape is calculated to be gaussian, which is in agreement with the fitting procedure assumptions. The model is used to determine the electron density range leading to the experimentally measured $\Delta\nu$. Uncertainties mainly arise from the small-signal gain and initial spontaneous emission power. However, the constraint of reaching the saturation regime reduces the effect of these uncertainties. The estimated electron densities for various pumping conditions are displayed in Table 2. For $\Phi = 22°$, $N_e$ is slightly lower than the $N_p$ values but still reasonable. Besides, the $N_e$ values for $\Phi = 32°$ are in very good agreement with the turning point density $N_p$.

**Table 2. Comparison with spectral line shape modelling for different grazing angle $\Phi$ and pulse duration $T_{IR}$ of the pumping pulse.**

| $\Phi(°)$ | $T_{IR}(ps)$ | $\Delta\nu(\times 10^{11} Hz)$ | $\tau_{FL}(ps)$ | $N_e(\times 10^{20} cm^{-3})$ |
|---|---|---|---|---|
| 32 | 4 | 5.3±0.5 | 0.8 ± 0.1 | 4.1 ±0.5 |
| 32 | 7 | 4.8±0.5 | 0.9 ± 0.1 | 4.0 ±0.1 |
| 22 | 4 | 2.8± 0.3 | 1.6 ± 0.2 | 2.0 ±0.2 |
| 22 | 7 | 2.0± 0.2 | 2.2 ± 0.3 | 0.6 ±0.2 |

For ASE XRL, the emitted pulse duration is governed by the gain dynamics. We compare the $\tau_{pulse}$ values presented in Table 1 to the results of a gain probing experiment. A seeded operation of XRL for $T_{IR} = 7ps$ at $\Phi = 22°$ and $T_{IR} = 4ps$ at $\Phi = 32°$ has been achieved. More details are provided in Appendix C and [9]. An auxiliary low-energy ($\leq$ 12 mJ) infrared beam of pulse duration $\sim 40fs$, is used to generate the HH seed in an Argon filled gas-cell. The seed source is placed $40mm$ before the entrance of the plasma. The 25th harmonic is spectrally, spatially and temporally matched with the amplifier. For a range of injection delays, an intense, and low

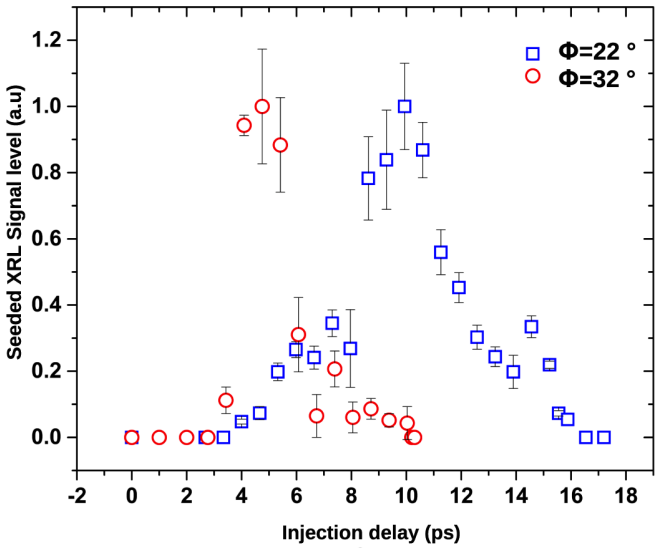


**Fig. 3.** Normalized seeded-XRL energy as a function of injection delays for low ($\Phi = 22°$ and $T_{IR} = 7ps$) and high ($\Phi = 32°$ and $T_{IR} = 4ps$) electron density amplifiers. In the high-density scenario, XRL plasma was seeded at an off-axis injection angle of $\sim 1°$ to counter the effects of refraction (see Appendix C). For both the configurations, the IR pump was delayed by $4ns$ with respect to the peak of preplasma forming pulse.

Optics EXPRESS

divergence seeded beam dominating the diverging ASE beam, is obtained. The normalized seeded-XRL intensity as a function of seed injection time is represented in Fig. 3 for both pumping angles. The injection temporal window during which seed is amplified is significantly shorter for $\Phi = 32°$ compared to $\Phi = 22°$; amplification window at FWHM for the respective cases are $2 \pm 0.5ps$ and $4.7 \pm 0.5ps$. The shorter amplification lifetime for higher $\Phi$ value is consistent with a larger electron density leading to a faster collisional ionization gating [1]. Furthermore, these amplification lifetimes are in agreement with the ASE pulse duration $\tau_{pulse}$ deduced from the temporal coherence analysis.

## 4. Seeded operation temporal coherence

In summary, the change in amplification dynamics and spectral behavior of the XRL from $\Phi = 22°$ to $\Phi = 32°$ is consistent with twice the increase of the electron density. This study demonstrates for the first time to our knowledge a controlled increase of the density in the gain region in seeded metal-target amplifiers under comparable pumping pulse irradiation parameters. Increasing the electron density is expected to lead to a shorter pulse duration in the seeded regime. We display in Table 2 the Fourier limited pulse duration $\tau_{FL} = \frac{2ln(2)}{\pi\Delta\nu}$ corresponding to the shortest pulse duration compatible with the gaussian spectrum of width $\Delta\nu$. For $\Phi = 32°$, the Fourier limit is below $1ps$. The prediction of the pulse structure and duration of a seeded-XRL is more complex due to the non-adiabatic response of the lasing species [15] and a Bloch-Maxwell description is required. However, the characteristic times involved in this evolution, namely the recovery time $T_1$, the dephasing rate $T_2$, and the pump duration $T_p$, are all connected to collisional effects and therefore inversely proportional to $N_e$. Besides, the temporal coherence analysis described in the previous section gives us quantitative constraints on these parameters.

We perform a one-dimensional Bloch-Maxwell simulation of the seeded-XRL pulse [16], where $T_2$ and $T_p$ were inferred from the experimental results previously described; further details on simulation is provided in Appendix F. Moreover, the seed intensity level was estimated experimentally, and $T_1$ was set from the value found in the literature [17].

The HH seed duration is set to $20fs$ [18]. The ratio between the seed intensity $I_{HH}$ and the XRL saturation intensity $I_{sat}$ is set to obtain an energy amplification close to the experimental one, for a small signal gain in the range $g = 50 - 100cm^{-1}$, typical for this kind of lasers [19,20]. The theoretical value of $I_{sat}$ was compared to an estimation of the ASE-XRL output intensity. The times $T_2$ and $T_p$ were deduced from the ASE temporal coherence measurements. More precisely, the dephasing time was assumed to be equal to $T_2 = 1/(\pi\Delta\nu_h)$ where $\Delta\nu_h$ is the homogeneous broadening calculated by the PPP code for electron density conditions displayed in Table 2. The FWHM pump duration $T_p$ was chosen to give a FWHM gain duration equal to two times $\tau_{pulse}$. The pertinence of this choice has been verified by numerically reproducing the injection window deduced from the HH seed injection delay scans; see Appendix F. Finally, the recovery time $T_1$ is set to $2ps$ following the experimental value reported in [17].

In Fig. 4 we show the simulation of seeded-XRL pulse properties after $L = 3mm$ propagation, with input parameters obtained in the case of $\Phi = 22°$ and $T_{IR} = 7ps$ (blue curves). The pulse temporal profiles are displayed in Fig. 4(a). The femtosecond harmonic seed (not visible here) is followed by a wake carrying most of the total energy, as described in [15]. From the corresponding field envelope, the simulated $|\gamma(\tau)|$ is calculated and is compared to experimentally measured fringe visibility for the seeded-XRL with $L = 3mm$, $\Phi = 22°$ and $T_{IR} = 7ps$ (black circles) in Fig. 4(b). The simulated $|\gamma(\tau)|$ has been normalized so that $|\gamma(0)| = V(0)$. The quasi-exponential decrease of the fringe visibility with delay is in very good agreement with the simulation. The FWHM duration of the corresponding pulse is predicted to be $\sim 1ps$. This value is close to the one measured by [21] for the same Ne-like Ti XRL amplifier and under similar pumping conditions.

Optics EXPRESS

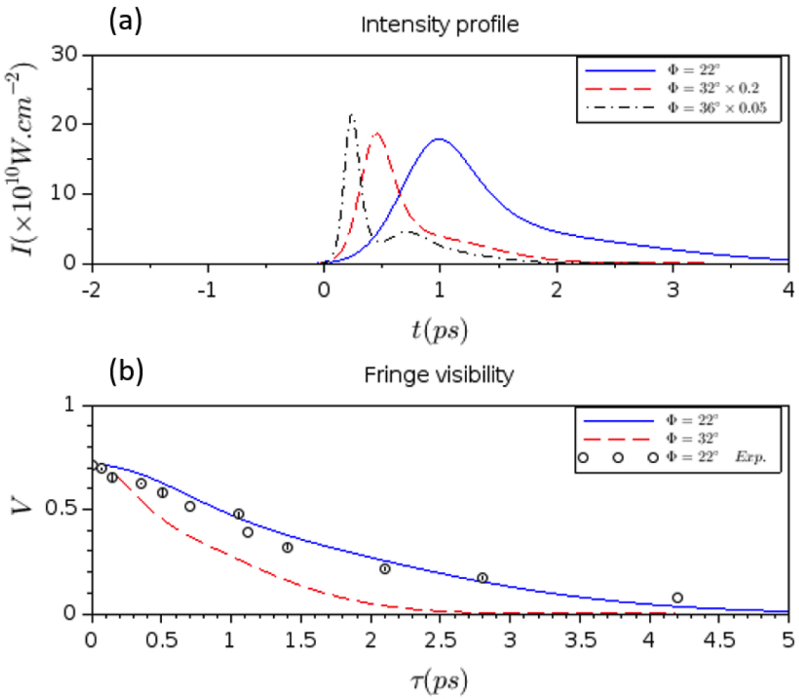


**Fig. 4.** Bloch-Maxwell simulation of the seeded-XRL operation. (a) The temporal intensity profile of the amplified pulse for $\Phi = 22°$, $L = 3mm$, and $T_{IR} = 7ps$ is shown in blue, whereas red-dashed curve shows the profile for $\Phi = 32°$, $L = 3mm$, and $T_{IR} = 4ps$. The extrapolated case $\Phi = 36°$, $L = 4mm$ is displayed in black. (b) Experimental (black circles) and simulated (solid blue line) fringe visibility for $\Phi = 22°$ and $T_{IR} = 7ps$. The red-dashed curve represents simulated fringe visibility for seeded-XRL pumped by $4ps$ pulse at $\Phi = 32°$. The simulated curves are scaled by the maximum value of the experimentally measured visibility for seeded-XRL.

## 5. Seeded operation at high densities

Higher electron densities are expected to increase beam refraction out of the amplifier and reduce the effective amplification length $L$. Strong refraction of the seeded beam has been observed experimentally for $\Phi = 32°$ pumping condition. Nevertheless, as explained in Appendix C, it was possible to mitigate this effect by optimizing the harmonic seed injection angle into the XRL plasma. An amplification length close to $L = 3mm$ was achieved, however, at a cost of consequential output beam angle. For $\Phi = 32°$ configuration, the seeded beam deflection was too important to be easily compensated to steer the beam towards the interferometer placed $\sim 3.2m$ further from the source. The given technical difficulty didn't allow the measurement of the temporal coherence properties of the seeded-XRL at this pumping angle. Nonetheless, we use the approach described above to simulate the pulse properties under given pumping conditions. We consider the same injection level as in the previous case, twice higher population inversion, and $L = 3mm$ amplification length. The results are displayed in Fig. 4 as dashed-red curves. The resulting pulse is expected to be four times more intense, with a FWHM pulse duration of $\sim 500fs$ for the main pulse, i.e., excluding the weaker wake signal. Besides, a larger spectral width and shorter pulse duration are also evident from a relatively faster decline of the simulated fringe visibility depicted by the red-dashed curve in Fig. 4(b).

Optics EXPRESS

Finally, we assess the potential of this amplifier to deliver even shorter and intense soft X-ray pulses. Considering an amplification length of $L = 4mm$, and a slightly higher grazing angle of $\Phi = 36°$, a pulse duration of $\sim 200fs$ at FWHM is attainable, primarily due to the manifestation of Rabi oscillations. This case is displayed in Fig. 4(a) by black curve. Howbeit, this potential will be reached with better mitigation strategies for refraction. Electron density gradient reduction by multiple pulse irradiation might be a path to explore. Using an element lasing in the same pumping conditions but at a shorter wavelength, such as Ni-like Mo, is another promising approach as it exhibits similar spectral width and gain duration properties [2] while the refraction effects are reduced with a $\sim 1/\lambda^2$ scaling.

## 6. Conclusion

In this paper, we have investigated the effect of a controlled increase of the electron density in the gain region of a plasma-based XRL on the gain bandwidth and output pulse duration simultaneously, using a linear autocorrelation measurement technique. Different pumping configurations expected to affect the electron density in the gain region were considered. We apply to these results, an analysis procedure derived from a statistical model of the ASE pulse. The benchmark on the model shows that it is possible to extract both the spectral linewidth and the pulse duration of the emitted field. The use of this procedure on experimental data demonstrates the ability of this model to represent the observed fringe visibility trends. Besides, the deduced bandwidth and pulse duration are in agreement with spectral models as well as seeded-XRL measurement results, respectively. These experimental data were used as input for Bloch-Maxwell simulation of the seeded-XRL operation. The simulated temporal coherence properties are in very good agreement with experimental results, and a seeded pulse duration of $\sim 1ps$ is predicted.

During this study, a high level of XRL lasing was achieved in conditions expected to increase the electron density in the gain region. We observed variation in the gain duration and spectral bandwidth consistent with twice an increase of the electron density. Moreover, we demonstrate that seeded operation was possible in this higher electron density case. We observed that the loss of gain-length product due to the strong refraction could be partially compensated by increasing the seed injection angle, at the price of technical beam-transport difficulties. Bloch-Maxwell simulations of the seeded operation in these conditions predict a pulse duration of $\sim 500fs$. These results predict that solid target plasma amplifier used routinely at high repetition rates, and offering a large variety of lasing wavelengths, can be utilized to deliver intense pulses with few hundreds of femtosecond pulse duration.

## Appendix A: description of wavefront-division interferometer

The measurements of temporal coherence were performed using a wavefront-division variable path-difference interferometer comprising a pair of dihedrons slightly tilted towards each other [22] and irradiated at 6° grazing incidence as depicted in Fig. 5. The small grazing angle facilitates good reflectivity for a large spectral window of the XUV beam. This arrangement splits the beam into two overlapping beamlets. Interference fringes formed in the overlapping zone are detected using an XUV CCD (ANDOR ikon-m BN, $13\mu m$ pixel size) with an inter-fringe spacing of $\sim 8$ pixels. A precision translation stage vertically displaces one of the dihedrons to induce a variable path difference $\delta$ between the interfering beams. The use of dihedron instead of a flat mirror ensures that the loss of fringe visibility is solely due to the finite temporal coherence and not resulting from a geometrical change in the beam overlap when $\delta$ is varied.

Optics EXPRESS

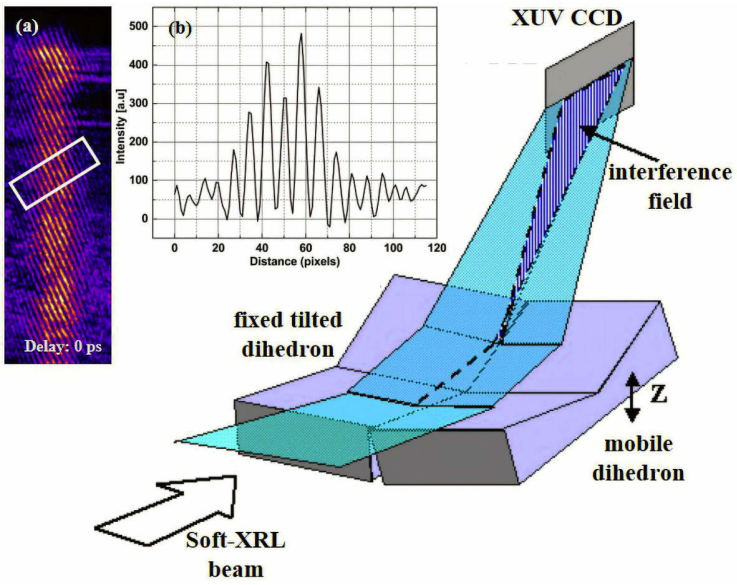


**Fig. 5.** Principle of wavefront-division variable path-difference interferometer comprising a dihedron pair. The hatched area represents the interference field. Inset figure (a) depicts a raw interferogram corresponding to a null delay for grazing incidence pumping angle of 32° and $T_{IR} = 4ps$. Line representation of the interferogram extracted from the region enclosed within the box (inset (a)) is presented in (b).

## Appendix B: visibility estimation

After subtracting the background from raw interferograms, the visibility is evaluated by applying a 3 fringes wide sliding-window fast Fourier transform (FFT) along the interfering zone. For a given window position, the local visibility is given by $V = 2(S_1/S_0)$, where $S_1$ and $S_0$ are the first and zero-order peak of the FFT signal in the spatial frequency domain. This yields a 2D map of the fringe visibility $V(x, y, \tau)$. For quasi-monochromatic radiation, the fringe visibility is related to the modulus of the complex degree of coherence through the relation $V(\tau) = R|\gamma(\tau)|$, where $R = 2\sqrt{I_1 I_2}/(I_1 + I_2)$ introduces a correction factor of <1 in case of unequal intensity in the interfering beamlets. Under the assumption of a constant spatial coherence within the sampled cross-section of the incident beam, the variation of visibility along the interfering zone is governed by inhomogeneous local intensity distribution within the two beams. As ASE-XRL exhibits structures on a spatial scale smaller than the overlapping zone, the resulting visibility map is non-uniform exhibiting deviations of ±10%. Therefore, for a given delay of $\tau$, the relevant and reported visibilities are the ones corresponding to $R = 1$. It is to note that $V(\tau = 0)$ remains below unity for partially coherent ASE-XRL as well as seeded-XRL that is expected to be fully coherent [23,24]. A similar observation has been reported before in the case of SASE-XFEL [25,26] and coherent high harmonic generated in rare gas [27]. For ASE-XRL and SASE-XFEL, such behavior reflects upon the commonality between the two sources: amplification of a random self-generated field that leads to an intense but partially coherent beam with limited spatial coherence. However, for a fully coherent seeded-XRL beam, $V(\tau = 0)$<1 is expected to arise from unequal intensity in the interfering beamlets and finite inter-fringe to detector pixel-size ratio [26,27].

Optics EXPRESS

## Appendix C: seeded operation of the XRL at high GRIP angle

A steep electron density gradient can strongly refract the injected high-harmonic seed out of the gain region, hence diminishing the gain-length product. While seeding high-density XRL plasma for $\Phi = 32^\circ$ grazing incidence pumping configuration, strong refraction of the seed was indeed observed. To counter the decrement of effective amplification length resulting from refraction, the injection angle of seed was varied. For a delay of 4*ns* between pre-plasma forming pulse and pump, the seed was injected 5.4*ps* following the peak intensity of the pump at various angles. The normalized seeded-XRL intensity for different seeding angles is presented in Fig. 6. A maximum signal level was observed for $1^\circ$ case. Consequently, the high-density amplifier (Fig. 3 of the main text) was seeded at this off-axis injection angle at different delays to probe the amplification dynamics of XRL.

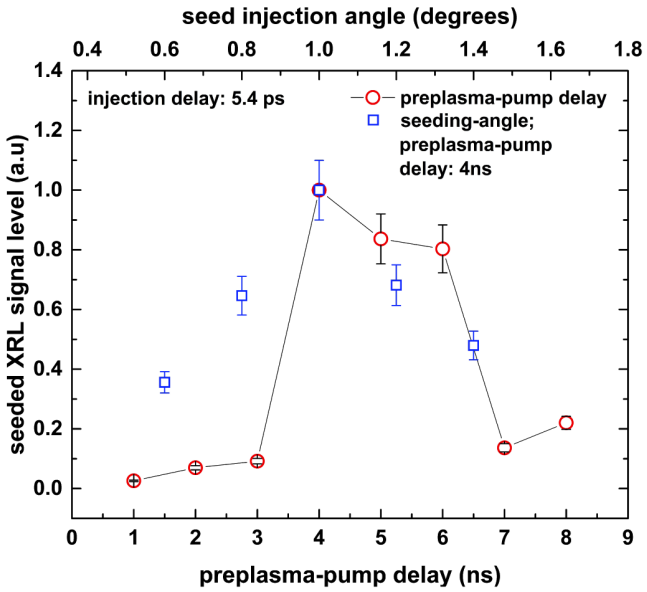


**Fig. 6.** Normalized seeded-XRL intensity as a function of delay between preplasma and pump pulse; high-harmonic seed is injected 5.4*ps* after the intensity peak of pump. For the given delay, most efficient amplification was observed for seeding angle of $1^\circ$.

## Appendix D: intrinsic linewidth

The soft X-ray laser theoretical line shape before amplification has been calculated using the PPP code [12,13]. The deduced FWHM linewidth is displayed in Fig. 7 for different electron density $N_e$ and temperature $T_e$ values. The homogeneous line profile calculation takes into account both the Stark effect and electron impact fields. The corresponding linewidths are displayed by dashed-lines. This profile is convoluted with a Doppler profile in order to give the total linewidth.

Optics EXPRESS

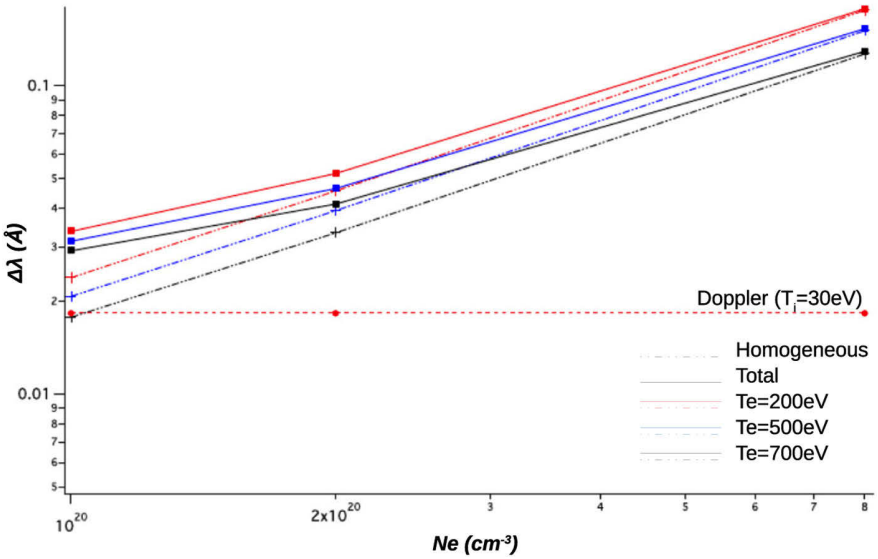


**Fig. 7.** Intrinsic linewidth (FWHM) of Ne-like Ti soft-XRL line as a function of the electron density $N_e$ for three levels of electron temperature $T_e$.

## Appendix E: validation of the coherence analysis procedure

The temporal coherence analysis of ASE XRL pulses has been tested on synthetic visibility curves, following the model proposed in [2]. These curves are obtained by an averaging procedure over a large number of numerically produced stochastic pulse profiles. The field $E(t)$ of a single pulse is the product of a stationary random field $E_s(t)$ by a gaussian envelope $E_g(t)$ of intensity FWHM $\tau_{pulse}$. The intensity spectrum $S(\nu)$ of $E_s$ is assumed to be gaussian and has a spectral bandwidth $\Delta\nu$. The stochastic temporal structure is obtained by doing the following hypothesis on the field spectral component $\tilde{E}_s(\nu)$ [11]: its modulus is $|\tilde{E}_s(\nu)| = \sqrt{S(\nu)}$ and its spectral phase $\phi(\nu)$ is a random number for each spectral channel. The Fourier transform of $\tilde{E}(\nu)$ will give the desired temporal structure for $E_s(t)$. A typical single pulse temporal profile is shown in Fig. 8(a), with a dotted curve representing the intensity envelope $|E_g(t)|^2$. The randomly placed spikes under this envelope have a temporal width inversely proportional to $\Delta\nu$. We represent in Fig. 8(b) the modulus of the simulated first-order degree of coherence function $|\gamma(\tau)|$ of this single pulse. The central part of this function can be approached by the Fourier transform of $S$, represented in red dotted line, which here is a gaussian of the form $|\gamma(\tau)| = h_0 exp(-(\tau/\tau_c)^2)$ with $\tau_c = 2\sqrt{ln(2)}/\pi\Delta\nu$, and $h_0 = 1$. However, far from $\tau = 0$, $|\gamma(\tau)|$ exhibits significant deviations to this gaussian curve, in the form of random fluctuations which are vanishing to zero on a time scale of the order of $\tau_{pulse}$. In our experiment, the data analysis is performed on an average of the visibility over many pulses. This situation is modeled by performing an average of $|\gamma(\tau)|$ on a large number $N$ of pulses. The result is noted $<|\gamma(\tau)|>$ and depicted in Fig. 8(c). The behavior for $\tau$ close to zero can still be modeled by the above-mentioned gaussian, still represented in red. However, for larger values of $\tau$, the random fluctuations are averaging in the form of a long pedestal, whose width is proportional to $\tau_{pulse}$. Note that this pedestal would be averaged to zero if the averaging operation was $|<\gamma(\tau)>|$. From these simulations, we tested that the pedestal can be modelled with a good accuracy by the following gaussian function: $|\gamma(\tau)| = h_1 exp(-log(2)(\tau/\tau_{pulse})^2)$. Moreover, it can be observed that the height of the pedestal $h_1$ decreases when $\tau_{pulse}$ is increased. In the limit of $\tau_{pulse} >> \tau_c$, the pedestal is negligible and $|<\gamma(\tau)>|$ is the Fourier transform of the stationnary field spectrum, as expected from the

Optics EXPRESS

Wiener-Khintchin theorem. Following Le Marec et al. [3], a relationship can be found between the height $h_1$ of the pedestal and the ratio $\tau_{pulse}/\tau_c$. We plot the ratio $h_1/h_0$ versus $\sqrt{\tau_c/\tau_{pulse}}$ in Fig. 8(d). A linear dependence is found with a slope $C = 0.71$ and a negligible offset. The application of these results to experimental data is straightforward. For each sampling point of $\tau$, the fringe visibility $V(\tau)$ is measured and averaged over several independent shots. The resulting data points hence are $<V(\tau)>$. Fitting the central part of $<V(\tau)>$ by a gaussian function provides access to $\Delta\nu$, whereas fitting the wings of $<V(\tau)>$ with another gaussian function yields the value of $\tau_{pulse}$. Of course, this procedure is meaningful only if the proposed model is pertinent to represent the ASE pulses. This pertinence can be further tested by the fact that the ratio $\tau_{pulse}/\tau_c$ should not only be encoded into the width of central part and wings but also in their heights.

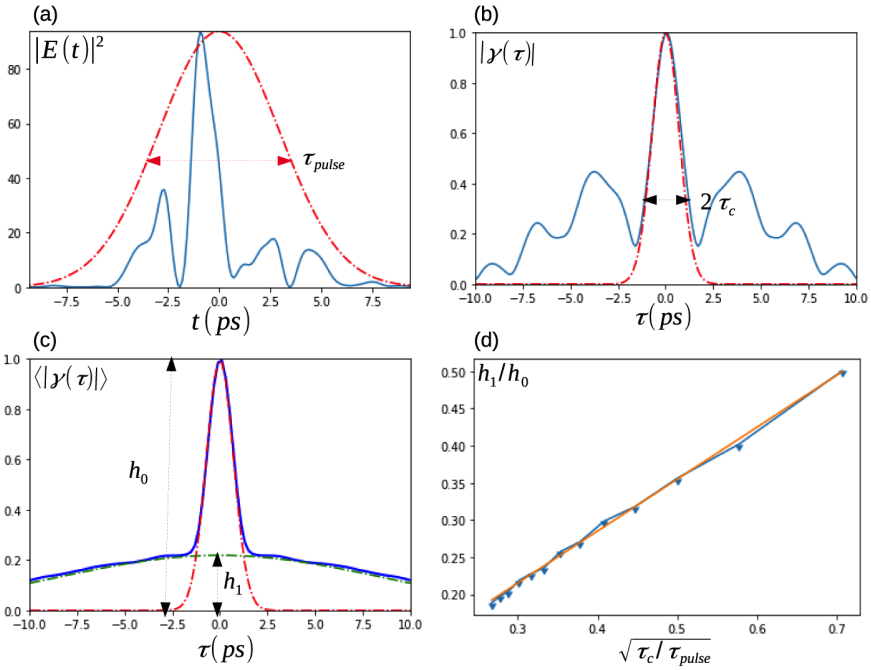


**Fig. 8.** ASE X-ray laser pulse modelling. (a) single-pulse temporal profile. Simulation of the modulus of its first-order autocorrelation function for (b) a single pulse (c) averaged over N=100 pulses. Fitting curves showed in red and green are presented in the main text. (d) The relationship between the different fitting parameters.

The consistency of this fitting procedure is therefore validated by forming the ratio $h_1/h_0$ of the heights of the two gaussian curves and verifying that its value is close to $C\sqrt{\tau_c/\tau_{pulse}}$.

## Appendix F: seeded operation modelling

The non-adiabatic response of the lasing dipole has to be taken into account in the description of the high harmonic seed amplification [15,28,29]. The harmonic seed is typically two orders of magnitude shorter than the inverse of the amplifier bandwidth while its peak intensity $I_{hhg}$ is close to the laser saturation intensity $I_{sat}$. In the present experiment, the high harmonic driving IR pulse duration is $\sim 40fs$. Due to the nonlinear response and transient conditions for phase matching, the harmonic pulse duration is shorter and is estimated to be $\tau_{HH} \sim 20fs$ assuming a low ionization level [18]. The seed peak intensity has been estimated from near-field images of the amplifier exit plane acquired using a high resolution, monochromatic extreme ultraviolet

Optics EXPRESS

(32.6$nm$) imaging system [4]. From these images, the HH beam size and photon count is extracted. The seed peak intensity and peak electric field are estimated to be $I_{hhg} = 1 \times 10^{10} W.cm^{-2}$ and $E_{hhg} = 2.7 \times 10^{8} V.m^{-1}$, respectively. Using the same diagnostics and $\tau_{pulse}$ value, an ASE peak intensity of $I_{ASE} = 2 \times 10^{10} W.cm^{-2}$ is obtained, which is expected to be slightly higher than $I_{sat}$.

A Bloch-Maxwell approach is required to simulate the coupled evolution of the soft X-ray field, the dipole density associated with the lasing transition, and the population inversion density. In the present situation, the harmonic seed is resonant with the X-ray laser line, and free-electron dispersion as well as absorption, are negligible. Reducing the problem to the spatial dimension $z$ along the amplifier axis and using the slowly varying envelope approximation, the following system of differential equations is solved numerically [16]:

$$\begin{aligned} \frac{\partial A}{\partial z} + \frac{1}{c}\frac{\partial A}{\partial t} &= D, \\ \frac{dD}{dt} &= -\frac{D}{T_2} + \frac{Z_0 \omega d^2}{2\hbar} AW, \\ \frac{dW}{dt} &= -\frac{(W - W_0(t))}{T_1} - \frac{3}{4\hbar\omega}\left(AD^* - A^* D\right). \end{aligned} \tag{1}$$

In the above set of equations, $A$ is the amplitude of the field envelope, $D$ is the dipole moment density of the medium, and $W$ is the population inversion. Here, $Z_0$ is the vacuum wave impedance so that the field intensity is $I = |A|^2$. The quantity $d^2$ is the squared modulus of the dipole matrix element. In the last expression of equation set (1), $W_0(t)$ is the equilibrium population inversion density that would be reached in the absence of the laser field. This term is driven by the incoherent pumping and depopulating rates of the lasing transition levels. The time dependence of $W_0(t)$ is assumed to be gaussian with a FWHM pump duration $T_p$ and a peak value $W_{0max}$. The level degeneracy is taken into account by a numerical factor preceding the last term of the third expression in Eq. (1) [16]. Finally, the characteristic times $T_1$ and $T_2$ are the recovery and dephasing times respectively; both are inversely proportional to the electron density $N_e$. These parameters are related to the small-signal gain at equilibrium $g_0$ and to the saturation intensity $I_{sat}$ by:

$$\begin{aligned} g_0 &= 2\alpha_0 T_2 W_0, \\ I_{sat} &= \frac{\hbar\omega}{2T_1 T_2 \alpha_0}, \\ \alpha_0 &= \frac{3 Z_0 d^2 \omega}{8\hbar}. \end{aligned} \tag{2}$$

To perform the simulations, the recovery time $T_1$ is set to $2ps$ and $1ps$ for $\Phi = 22°$ and $\Phi = 32°$ respectively; the first value being close to the experimental measurements reported in [17]. We set $T_2 = \dfrac{1}{\pi \Delta\nu_h}$, where $\Delta\nu_h$ is the homogeneous linewidth predicted by the PPP simulation [12,13] and leading to the best agreement with ASE-XRL experimental bandwidth (Table 2 of the main text). The dipole $d^2$ is deduced from MCDF atomic structure codes [30]. With these input parameters, a theoretical saturation intensity of $I_{sat} = 5 \times 10^{9} W.cm^{-2}$ is found, whose order of magnitude is in agreement with the experimental estimation. The peak value of the population inversion $W_{0max}$ has been estimated using the typical values of the small-signal gain $g_0$ published in the literature for this kind of amplifier [19,20]: $50cm^{-1} < g_0 < 100cm^{-1}$, consistent with a saturated laser for $L \sim 2 - 3mm$. Finally, the pump duration $T_p$ is assumed to be equal to $\sim 1.5\tau_{pulse}$, where $\tau_{pulse}$ is deduced from the experimental measurements (Table 1 of the main text). This choice leads to an instantaneous population inversion $W(t)$ lasting $\sim 2\tau_{pulse}$.

With the given set of parameters and an amplification length of $L = 3mm$, the seeded pulse reaches the saturation regime. As displayed in Fig. 9(a), the population $W$, is strongly depopulated by the pulse intensity and recovers on a time scale of $T_1$. Under the given situation relevant to the experiment, no population oscillation resulting from Rabi flopping is observed. However, for an amplification length of $L = 4mm$, this phenomenon is expected. The pulse spectrum of the

Optics EXPRESS

seeded-XRL has also been calculated and is depicted in Fig. 9(b). Additionally, we display the ASE-XRL spectrum deduced from temporal coherence measurement for $\Phi = 22°$, $T_{IR} = 7ps$ in the same figure. In comparison to the spectrum of seeded-XRL, the gaussian lineshape with FWHM width $\Delta\nu$ is in reasonable agreement regarding the central part, but differ significantly in the wings. The wings of the seeded-XRL simulated spectrum grow with stronger amplification leading ultimately to Rabi oscillations. Therefore, inferring the shortest seeded pulse duration accessible with an amplifier through its ASE bandwidth is reasonable only when the seeded operation is close to saturation.

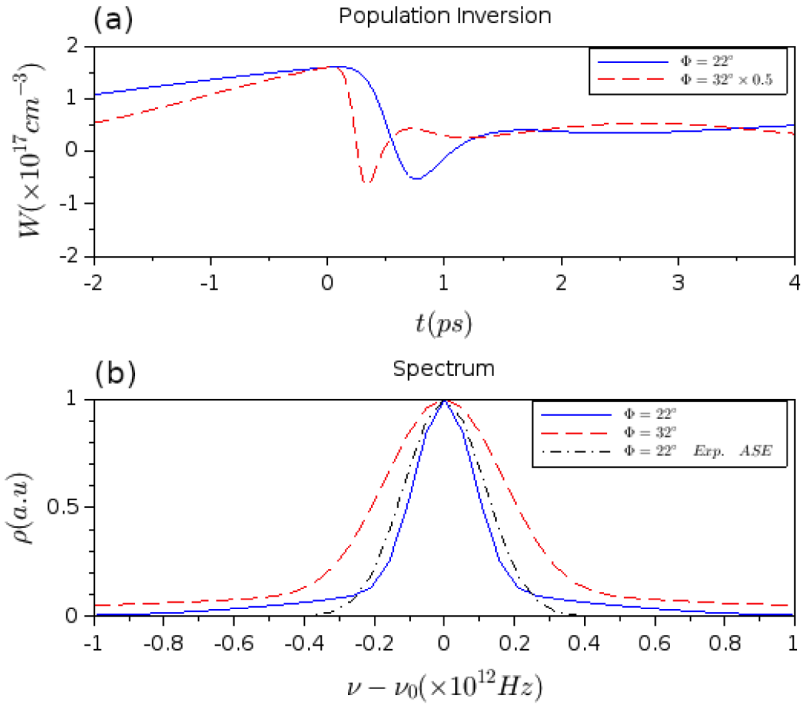


**Fig. 9.** Bloch-Maxwell simulation of the XRL seeded operation for $\Phi = 22°$, $T_{IR} = 7ps$ and $\Phi = 32°$, $T_{IR} = 4ps$. (a) shows population inversion under aforementioned conditions. The simulated spectra of the seeded XRL for both configurations, along with the ASE-XRL spectrum obtained from experimental coherence measurement for $\Phi = 22°$, $T_{IR} = 7ps$ is presented in (b) by dashed-black curve.

Finally, to assess the pertinence of the postulated pump duration $T_p$, we simulate the harmonic seed amplification for different injection times. The temporal profile of the population inversion $W(t)$, is displayed in Fig. 10 by the black curve, whereas the output energy as a function of injection delays is presented in blue. A reasonable agreement with the experimentally probed amplification dynamics presented in Fig. 3 of the main text, is obtained for both the configurations.

Optics EXPRESS

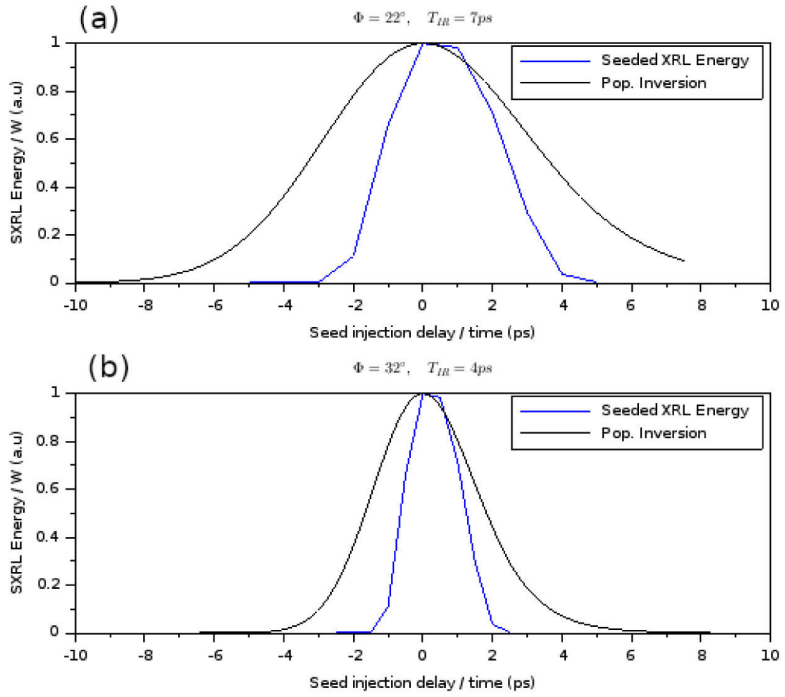


**Fig. 10.** Bloch-Maxwell simulation of the XRL seeded output energy for different seed injection delays (blue curves) for input parameters corresponding to $\Phi = 22°$, $T_{IR} = 7ps$ (a) and $\Phi = 32°$, $T_{IR} = 4ps$ (b). Evolution of the population inversion in the absence of laser field is plotted in black.

## Funding

Université Paris-Saclay (2012-0333T-OASIS, 50110000724-OPTX); Conseil Régional, Île-de-France (501100003990); Laserlab-Europe (284464).

## Acknowledgement

The authors acknowledge the Centrale d'Elaboration et de Métrologie des Optiques XUV (CEMOX) installation at Institut d'Optique Graduate School (IOGS), Palaiseau, France, for providing the multilayer optics. The authors thank ISMO and IJC Lab technical staff. Authors are thankful to Fabien Tissandier for fruitful discussions.

## Disclosures

The authors declare no conflicts of interest.

## References

1. A. Depresseux, E. Oliva, J. Gautier, F. Tissandier, J. Nejdl, M. Kozlova, G. Maynard, J. P. Goddet, A. Tafzi, A. Lifschitz, H. T. Kim, S. Jacquemot, V. Malka, K. Ta Phuoc, C. Thaury, P. Rousseau, G. Iaquaniello, T. Lefrou, A. Flacco, B. Vodungbo, G. Lambert, A. Rousse, P. Zeitoun, and S. Sebban, "Table-top femtosecond soft x-ray laser by collisional ionization gating," Nat. Photonics **9**(12), 817–821 (2015).
2. A. L. Marec, O. Guilbaud, O. Larroche, and A. Klisnick, "Evidence of partial temporal coherence effects in the linear autocorrelation of extreme ultraviolet laser pulses," Opt. Lett. **41**(14), 3387–3390 (2016).
3. A. L. Marec, O. Larroche, and A. Klisnick, "Linear autocorrelation of partially coherent extreme-ultraviolet lasers: a quantitative analysis," Opt. Lett. **42**(23), 4958–4961 (2017).

Optics EXPRESS


4. O. Delmas, M. Pittman, K. Cassou, O. Guilbaud, S. Kazamias, G. V. Cojocaru, O. Neveu, J. Demailly, E. Baynard, D. Ursescu, and D. Ros, "Q-switched laser-assisted grazing incidence pumping (qagrip) for efficient soft x-ray laser generation," Opt. Lett. **39**(21), 6102–6105 (2014).
5. Y. V. Afanas'ev and V. N. Shlyaptsev, "Formation of a population inversion of transitions in ne-like ions in steady-state and transient plasmas," Sov. J. Quantum Electron. **19**(12), 1606–1612 (1989).
6. V. N. Shlyaptsev, P. V. Nickles, T. Schlegel, M. P. Kalachnikov, and A. L. Osterheld, "Tabletop x-ray laser pumped with subnanosecond and picosecond pulses," in *Ultrashort Wavelength Lasers II*, vol. 2012 S. Suckewer, ed., International Society for Optics and Photonics (SPIE, 1994), pp. 111–118.
7. P. V. Nickles, V. N. Shlyaptsev, M. Kalachnikov, M. Schnürer, I. Will, and W. Sandner, "Short pulse x-ray laser at 32.6 nm based on transient gain in ne-like titanium," Phys. Rev. Lett. **78**(14), 2748–2751 (1997).
8. J. Dunn, A. I. Osterheld, Y. Li, J. Nilsen, and V. N. Shlyaptsev, "Transient collisional excitation x-ray lasers with 1-ps tabletop drivers," IEEE J. Sel. Top. Quantum Electron. **5**(6), 1441–1446 (1999).
9. O. Guilbaud, G. V. Cojocaru, L. Li, O. Delmas, R. G. Ungureanu, R. A. Banici, S. Kazamias, K. Cassou, O. Neveu, J. Demailly, E. Baynard, M. Pittman, A. L. Marec, A. Klisnick, P. Zeitoun, D. Ursescu, and D. Ros, "Gain dynamics in quickly ionized plasma for seeded operated soft x-ray lasers," Opt. Lett. **40**(20), 4775–4778 (2015).
10. R. Keenan, J. Dunn, P. K. Patel, D. F. Price, R. F. Smith, and V. N. Shlyaptsev, "High-repetition-rate grazing-incidence pumped x-ray laser operating at 18.9 nm," Phys. Rev. Lett. **94**(10), 103901 (2005).
11. T. Pfeifer, Y. Jiang, S. Düsterer, R. Moshammer, and J. Ullrich, "Partial-coherence method to model experimental free-electron laser pulse statistics," Opt. Lett. **35**(20), 3441–3443 (2010).
12. A. Calisti, F. Khelfaoui, R. Stamm, B. Talin, and R. W. Lee, "Model for the line shapes of complex ions in hot and dense plasmas," Phys. Rev. A **42**(9), 5433–5440 (1990).
13. E. Galtier, F. B. Rosmej, A. Calisti, B. Talin, C. Mossé, S. Ferri, and V. S. Lisitsa, "Interference effects and stark broadening in xuv intrashell transitions in aluminum under conditions of intense xuv free-electron-laser irradiation," Phys. Rev. A **87**(3), 033424 (2013).
14. J. A. Koch, B. J. MacGowan, L. B. Da Silva, D. L. Matthews, J. H. Underwood, P. J. Batson, and S. Mrowka, "Observation of gain-narrowing and saturation behavior in se x-ray laser line profiles," Phys. Rev. Lett. **68**(22), 3291–3294 (1992).
15. I. R. Al'miev, O. Larroche, D. Benredjem, J. Dubau, S. Kazamias, C. Möller, and A. Klisnick, "Dynamical description of transient x-ray lasers seeded with high-order harmonic radiation through maxwell-bloch numerical simulations," Phys. Rev. Lett. **99**(12), 123902 (2007).
16. F. Tissandier, S. Sebban, J. Gautier, P. Zeitoun, E. Oliva, A. Rousse, and G. Maynard, "Three-dimensional maxwell-bloch calculation of the temporal profile of a seeded soft x-ray laser pulse," Appl. Phys. Lett. **101**(25), 251112 (2012).
17. Y. Wang, S. Wang, E. Oliva, L. Li, M. Berrill, L. Yin, J. Nejdl, B. M. Luther, C. Proux, T. T. T. Le, J. Dunn, D. Ros, P. Zeitoun, and J. J. Rocca, "Gain dynamics in a soft-x-ray laser amplifier perturbed by a strong injected x-ray field," Nat. Photonics **8**(5), 381–384 (2014).
18. J. Mauritsson, P. Johnsson, R. López-Martens, K. Varjú, W. Kornelis, J. Biegert, U. Keller, M. B. Gaarde, K. J. Schafer, and A. L'Huillier, "Measurement and control of the frequency chirp rate of high-order harmonic pulses," Phys. Rev. A **70**(2), 021801 (2004).
19. Y. Wang, M. A. Larotonda, B. M. Luther, D. Alessi, M. Berrill, V. N. Shlyaptsev, and J. J. Rocca, "Demonstration of high-repetition-rate tabletop soft-x-ray lasers with saturated output at wavelengths down to 13.9 nm and gain down to 10.9 nm," Phys. Rev. A **72**(5), 053807 (2005).
20. H. T. Kim, I. W. Choi, N. Hafz, J. H. Sung, T. J. Yu, K.-H. Hong, T. M. Jeong, Y.-C. Noh, D.-K. Ko, K. A. Janulewicz, J. Tümmler, P. V. Nickles, W. Sandner, and J. Lee, "Demonstration of a saturated ni-like ag x-ray laser pumped by a single profiled laser pulse from a 10-hz ti:sapphire laser system," Phys. Rev. A **77**(2), 023807 (2008).
21. Y. Wang, M. Berrill, F. Pedaci, M. M. Shakya, S. Gilbertson, Z. Chang, E. Granados, B. M. Luther, M. A. Larotonda, and J. J. Rocca, "Measurement of 1–ps soft-x-ray laser pulses from an injection-seeded plasma amplifier," Phys. Rev. A **79**(2), 023810 (2009).
22. F. Polack, D. Joyeux, J. Svatoš, and D. Phalippou, "Applications of wavefront division interferometers in soft x rays," Rev. Sci. Instrum. **66**(2), 2180–2183 (1995).
23. Y. Wang, E. Granados, F. Pedaci, D. Alessi, B. Luther, M. Berrill, and J. J. Rocca, "Phase-coherent, injection-seeded, table-top soft-x-ray lasers at 18.9 nm and 13.9 nm," Nat. Photonics **2**(2), 94–98 (2008).
24. O. Guilbaud, F. Tissandier, J.-P. Goddet, M. Ribière, S. Sebban, J. Gautier, D. Joyeux, D. Ros, K. Cassou, S. Kazamias, A. Klisnick, J. Habib, P. Zeitoun, D. Benredjem, T. Mocek, J. Nedjl, S. de Rossi, G. Maynard, B. Cros, A. Boudaa, and A. Calisti, "Fourier-limited seeded soft x-ray laser pulse," Opt. Lett. **35**(9), 1326–1328 (2010).
25. R. Mitzner, B. Siemer, M. Neeb, T. Noll, F. Siewert, S. Roling, M. Rutkowski, A. Sorokin, M. Richter, P. Juranic, K. Tiedtke, J. Feldhaus, W. Eberhardt, and H. Zacharias, "Spatio-temporal coherence of free electron laser pulses in the soft x-ray regime," Opt. Express **16**(24), 19909–19919 (2008).
26. S. Roling, B. Siemer, M. Wöstmann, H. Zacharias, R. Mitzner, A. Singer, K. Tiedtke, and I. A. Vartanyants, "Temporal and spatial coherence properties of free-electron-laser pulses in the extreme ultraviolet regime," Phys. Rev. Spec. Top.–Accel. Beams **14**(8), 080701 (2011).

Optics EXPRESS

27. J. Terschlüsen, M. Agåker, M. Svanqvist, S. Plogmaker, J. Nordgren, J.-E. Rubensson, H. Siegbahn, and J. Söderström, "Measuring the temporal coherence of a high harmonic generation setup employing a fourier transform spectrometer for the vuv/xuv," Nucl. Instrum. Methods Phys. Res., Sect. A **768**, 84–88 (2014).
28. C. M. Kim, J. Lee, and K. A. Janulewicz, "Coherent amplification of an ultrashort pulse in a high- and swept-gain medium with level degeneracy," Phys. Rev. Lett. **104**(5), 053901 (2010).
29. O. Larroche, D. Ros, A. Klisnick, A. Sureau, C. Möller, and H. Guennou, "Maxwell-bloch modeling of x-ray-laser-signal buildup in single- and double-pass configurations," Phys. Rev. A **62**(4), 043815 (2000).
30. I. Grant, B. McKenzie, P. Norrington, D. Mayers, and N. Pyper, "An atomic multiconfigurational dirac-fock package," Comput. Phys. Commun. **21**(2), 207–231 (1980).